


Article

NH₃ Sensor Based on 3D Hierarchical Flower-Shaped *n*-ZnO/*p*-NiO Heterostructures Yields Outstanding Sensing Capabilities at ppb Level

Zhenting Zhao ^{1,2}, Haoyue Yang ², Zihan Wei ³, Yan Xue ², Yongjiao Sun ², Wenlei Zhang ², Pengwei Li ², Weiping Gong ¹ , Serge Zhuiykov ³ and Jie Hu ^{2,*}

¹ Guangdong Provincial Key Laboratory of Electronic Functional Materials and Devices, Huizhou University, Huizhou 516001, Guangdong, China; zhzhenting@hzu.edu.cn (Z.Z.); gwp@hzu.edu.cn (W.G.)

² Center of Nano Energy and Devices, College of Information and computer, Taiyuan University of Technology, Taiyuan 030024, Shanxi, China; yanghaoyue0220@link.tyut.edu.cn (H.Y.); xueyan0179@link.tyut.edu.cn (Y.X.); sunyongjiao@tyut.edu.cn (Y.S.); zhangwenlei@tyut.edu.cn (W.Z.); lipengwei@tyut.edu.cn (P.L.)

³ Department of Solid State Science, Faculty of Science, Ghent University Global Campus, 119 Songdomunhwa-ro, Yeonsu-gu, Incheon 21985, Korea; zihan.wei@ugent.be (Z.W.); serge.zhuiykov@ghent.ac.kr (S.Z.)

* Correspondence: hujie@tyut.edu.cn

Received: 5 August 2020; Accepted: 20 August 2020; Published: 22 August 2020



Abstract: Hierarchical three-dimensional (3D) flower-like *n*-ZnO/*p*-NiO heterostructures with various Zn_xNi_y molar ratios (Zn₅Ni₁, Zn₂Ni₁, Zn₁Ni₁, Zn₁Ni₂ and Zn₁Ni₅) were synthesized by a facile hydrothermal method. Their crystal phase, surface morphology, elemental composition and chemical state were comprehensively investigated by XRD, SEM, EDS, TEM and XPS techniques. Gas sensing measurements were conducted on all the as-developed Zn_xNi_y-based sensors toward ammonia (NH₃) detection under various working temperatures from 160 to 340 °C. In particular, the as-prepared Zn₁Ni₂ sensor exhibited superior NH₃ sensing performance under optimum working temperature (280 °C) including high response (25 toward 100 ppm), fast response/recovery time (16 s/7 s), low detection limit (50 ppb), good selectivity and long-term stability. The enhanced NH₃ sensing capabilities of Zn₁Ni₂ sensor could be attributed to both the specific hierarchical structure which facilitates the adsorption of NH₃ molecules and produces much more contact sites, and the improved gas response characteristics of *p*-*n* heterojunctions. The obtained results clear demonstrated that the optimum *n*-ZnO/*p*-NiO heterostructure is indeed very promising sensing material toward NH₃ detection for different applications.

Keywords: hierarchical structures; NH₃ sensing properties; *n*-ZnO/*p*-NiO heterojunction; gas sensor; ammonia

1. Introduction

It is common knowledge that ammonia (NH₃) is one of the most widely produced industrial chemicals, which plays an important role in manufacturing systems such as dyes, drugs, plastics, etc. [1]. Moreover, NH₃ is also easily found in our daily life, including the dairy and ice cream plants, wineries and breweries, and juice and drink processing [2]. However, it should be noticed that NH₃, as strongly irritating gas, is not only flammable under the concentrations of 16–28 vol % in air, but also exhibit highly toxic and hazardous effects on the ecosystem and human health [3–5]. For humans, the acute exposure to NH₃ may cause severe health problems, such as headaches, nausea, and intense burning of the skin, eyes, throat and nose. Moreover, if interactions with high concentration of gaseous

NH₃ take place for a long time, people will suffer from serious pharyngeal pain, chest tightness, dyspnea, toxic phenomena and even death [6]. According to the recommendation of National Institute for Occupational Safety and Health (NIOSH), the threshold limit value of NH₃ should be below 25 ppm in the work environments place [2]. Therefore, it is highly desirable and essential to develop high performance sensors for NH₃ detection at the low concentration level for industrial, agricultural and health monitoring applications.

Recently, metallic oxide semiconductor (MOS), such as ZnO [7], SnO₂ [8], NiO [9], WO₃ [10], In₂O₃ [11], etc. have extensively studied for constructing gas sensors, because of their advantages of environmental protection, low price, fast response speed to flammable and organic volatile gases [12,13]. Nevertheless, the most of MOS based sensors still face many drawbacks such as low sensitivity, high working temperature and poor reliability and selectivity, which might block their industrial applications. Thus, to improve further gas sensing performance of the MOS based sensors, different approaches were adopted and implemented including but not limited to the morphology controlling [14,15], doping with suitable nanometals [16,17] and formation heterojunctions and heterointerfaces [18,19]. Among these methods, heterojunction construction, which forms at the interface between the different MOS, is one of the most effective strategies for enhancement of gas sensing properties. Moreover, construction of heterojunction semiconductor provides an important way to combine the different properties of each single component into one combined system [20]. In addition, the heterostructured MOS based sensing materials have also the features of finer grains, enhanced surface-to-volume ratio and increased gas accessibility.

Zinc oxide (ZnO), as a typical *n*-type semiconductor sensing material, has attracted great attention because of its good gas sensing performance [7,21,22]. Up to now, many working groups tried to improve the gas sensing properties of ZnO-based gas sensors by construction *p-n* heterojunctions. For example, Chen et al. reported the fabrication of ultraporous ZnO/NiO heterojunction networks using flame synthesis and aerosol self-assemble, and studied their gas sensitivity toward volatile organic compounds (VOC) gas [23]. The reported results demonstrated that the ZnO/NiO nanoparticle networks demonstrated excellent sensitivity to acetone and ethanol gas. Kaur et al. fabricated NiO/ZnO one-dimensional nanowire, in which the NiO nanowires act as backbones for the growth of ZnO [24]. The hybrid nanostructures showed enhanced VOC gas sensing behavior compared to NiO sensors. Moreover, Zhou et al. prepared the nanodisk-shaped NiO/ZnO-based SO₂ gas sensor, and the obtained gas response can reach to 16.25 [25]. Notwithstanding many previous works reporting great gas sensing properties of ZnO/NiO heterojunction structures for detection of the different gases, to the best of our knowledge, the optimization Zn:Ni content and its corresponding sensing performance towards NH₃ has not yet been done. Therefore, there is much room for the synthesis and development of *n-ZnO/p-NiO* based NH₃ sensors with superior sensing properties.

In the present work, we report systematic studies with respect to the effect of ZnO/NiO *p-n* heterojunctions on the NH₃ sensing. For this purpose, a series of *n-ZnO/p-NiO* hierarchical structures with different Zn:Ni molar ratios (Zn_{*x*}Ni_{*y*}) were successfully synthesized using the one-pot hydrothermal route and then systematically characterized. Gas sensing measurements were carried out on all the as-developed Zn_{*x*}Ni_{*y*}-based sensors towards NH₃ detection. After comprehensive studies, it was found that the different heterojunction proportions can greatly affect the gas-sensing performance. The measured results proved and confirmed that the as-prepared Zn₁Ni₂ sensor exhibited the best gas sensing performance for NH₃ at the selected optimum working temperature of 280 °C, and consequently, demonstrated that the 3D *n-ZnO/p-NiO* heterostructure is a very promising sensing material for NH₃ sensors with superior capabilities at low ammonia concentrations.

2. Materials and Methods

2.1. Chemicals and Reagents

Zinc acetate dihydrate ($\text{Zn}(\text{CH}_3\text{COO})_2 \cdot 2\text{H}_2\text{O}$, $\geq 99.9\%$), Nickel(II) acetate tetrahydrate ($\text{Ni}(\text{CH}_3\text{COO})_2 \cdot 4\text{H}_2\text{O}$, $\geq 99.0\%$), Glycine ($\text{NH}_2\text{CH}_2\text{COOH}$, $\geq 99.0\%$), and Ammonium bicarbonate (NH_4HCO_3 , $\geq 99.0\%$) were purchased from Sigma-Aldrich (Shanghai, China). All chemical reagents in the experiments were of analytical grade and used as received without further purification. The deionized water (DI water, $18.25 \text{ M}\Omega\text{-cm}$) used in all experiments was prepared with a Milli-Q water purification system (Milli-Q HX 7000, Merck KGaA, Darmstadt, Germany).

2.2. Synthesis of ZnO/NiO Hierarchical Structures

3D hierarchical structures of *n*-ZnO/*p*-NiO heterojunctions were synthesized by one-pot hydrothermal method. Typically, 16 mmol NH_4HCO_3 was dissolved into 40 mL DI water for formation an aqueous solution. Then 16 mmol $\text{NH}_2\text{CH}_2\text{COOH}$, different molar ratio of $\text{Zn}(\text{CH}_3\text{COO})_2 \cdot 2\text{H}_2\text{O}$ and $\text{Ni}(\text{CH}_3\text{COO})_2 \cdot 4\text{H}_2\text{O}$ (Zn:Ni = 5:1, 2:1, 1:1, 1:2, 1:5) were dissolved into another 40 mL DI water with magnetic stirring for 1 h at the room temperature. After that, the obtained NH_4HCO_3 solution was added into the above solution, and transferred into 100 mL Teflon-lined stainless-steel autoclave. Then, after 3 h of reaction at $180 \text{ }^\circ\text{C}$, the resulting product was collected via centrifugation, washing and drying. Finally, the obtained product was annealed at $500 \text{ }^\circ\text{C}$ for 2 h in air for structural stabilization. Additionally, the 3D hierarchical flower-like *n*-ZnO/*p*-NiO heterostructures with the different Zn:Ni molar ratios were also synthesized for comparison and marked as Zn_5Ni_1 , Zn_2Ni_1 , Zn_1Ni_1 , Zn_1Ni_2 and Zn_1Ni_5 , respectively. The as-synthesized samples were stored in the dry environment at room temperature for subsequent experiments.

2.3. Material Characterization

The structure and the phase of the sample were evaluated by X-ray diffraction (XRD, D/MAX-2500 V/PC, Rigaku, Japan). The microstructures of as-synthesized 3D flower-like *n*-ZnO/*p*-NiO hierarchical structures were analyzed by scanning electron microscopy (SEM, JSM-7100F, JEOL, Japan) and their crystalline structures were further confirmed by transmission electron microscopy (TEM, JEM-2100, JEOL, Japan). Furthermore, the surface compositions and chemical state of samples were examined by X-ray photoelectron spectroscopy (XPS, ESCALAB 250Xi, Thermo Fisher Scientific, Waltham, MA, USA).

2.4. Gas Sensors Fabrication and Measurement

The gas sensors were fabricated by pasting the as-synthesized 3D flower-like *n*-ZnO/*p*-NiO hierarchical structures on the interdigitated electrode (IDE). The IDE was prepared by making interdigital gold electrode on the glass substrate by photolithography and magnetron sputtering techniques. To improve its stability, the *n*-ZnO/*p*-NiO modified IDE-based sensing electrodes were transferred to aging stage with 5 V for 3 days. Chemiresistive properties of the 3D *n*-ZnO/*p*-NiO heterostructures were evaluated using CGS-1TP intelligent analysis system (Elite, Beijing, China) under the laboratory conditions ($30 \pm 3\% \text{ RH}$, $25 \pm 2 \text{ }^\circ\text{C}$). The schematic diagram of the gas sensor testing system used in our investigation is shown in Figure 1. The response is defined as R_a/R_g (R_a is the sensor resistance in air and R_g reflects the resistance in the targeted gas). We defined the time of the sensor to reach 90% of the total resistance change as the response and recovery time (τ_{res} and τ_{rec}), respectively.

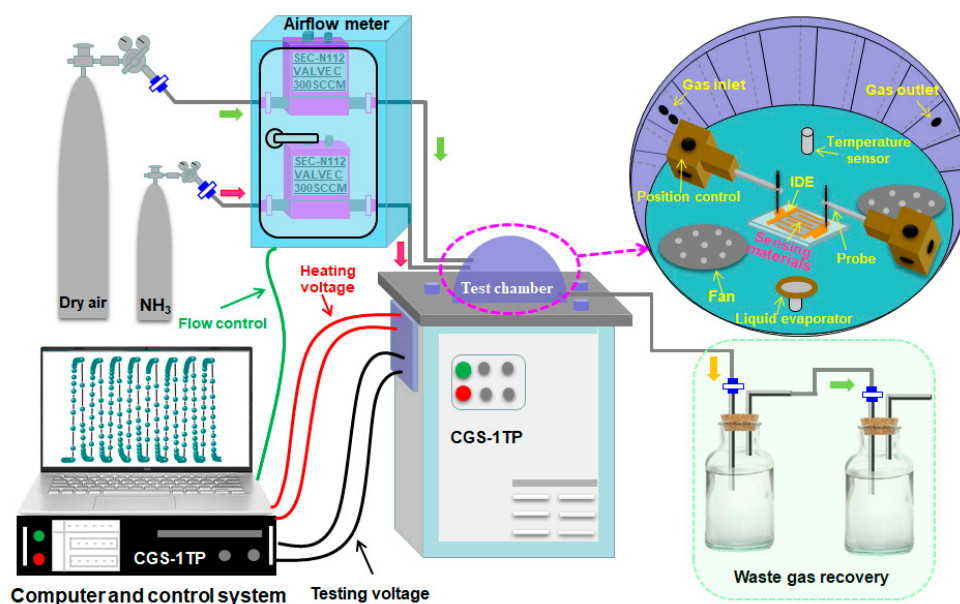


Figure 1. Schematic diagram of gas sensors testing system.

3. Results

3.1. Structure and Morphology Characterization

The crystal structures of as-synthesized 3D flower-like n -ZnO/ p -NiO nanocomposites were investigated by XRD and the main results are depicted in Figure 2a, where all the diffraction peaks marked with (*) can be indexed to the patterns of ZnO (JCPDS-36-1451). And the peaks located at $2\theta = 31.68^\circ, 34.42^\circ, 36.25^\circ, 37.45^\circ, 56.57^\circ, 62.81^\circ, 66.30^\circ, 67.92^\circ, 69.05^\circ$ and 76.95° can be indexed to the (100), (002), (101), (102), (110), (103), (200), (112), (201) and (202) planes of ZnO. However, with the increasing Ni molar ratio Figure 2b–e, the XRD patterns of NiO (marked with #) appeared for Zn_2Ni_1 , Zn_1Ni_1 , Zn_1Ni_2 and Zn_1Ni_5 samples. The planes can be ascribed to the standard XRD patterns of NiO (JCPDS-47-1049). Meanwhile, the intensity of diffraction peaks related to (111), (200) and (311) planes of NiO get stronger and sharper with the increasing proportion of Ni, confirming the existence of NiO in the heterostructures. Moreover, there are no other characteristic peaks were detected for all n -ZnO/ p -NiO hierarchical structures, and thus the obtained results demonstrated high purity of as-synthesized samples.

The morphology of all the as-synthesized 3D n -ZnO/ p -NiO hierarchical structure was investigated by scanning electron microscopy (SEM). Figure 3a–e shows the SEM images of the n -ZnO/ p -NiO composites, which were prepared by the different Zn-to-Ni molar ratio. It appears to indicate that all samples possess 3D flower-like hierarchical microstructure. The diameter of the individual flower is about $3.5 \pm 0.5 \mu\text{m}$. Furthermore, the insets in Figure 3a–e show the high magnification SEM images of the single nanostructure. It can be observed that the flower-like n -ZnO/ p -NiO is self-assembled by aggregation of many nanosheets, and the Zn_1Ni_2 possesses the largest distance between the nanosheets, which will facilitate exposure to the target gas. Moreover, the elemental composition of Zn_1Ni_2 hierarchical structures was determined using EDS analysis. Specifically, Figure 3f shows the elemental mapping images of a typical Zn_1Ni_2 hierarchical structure, clearly representing the distribution of Zn, Ni, and O elements in the 3D flower-like structure.

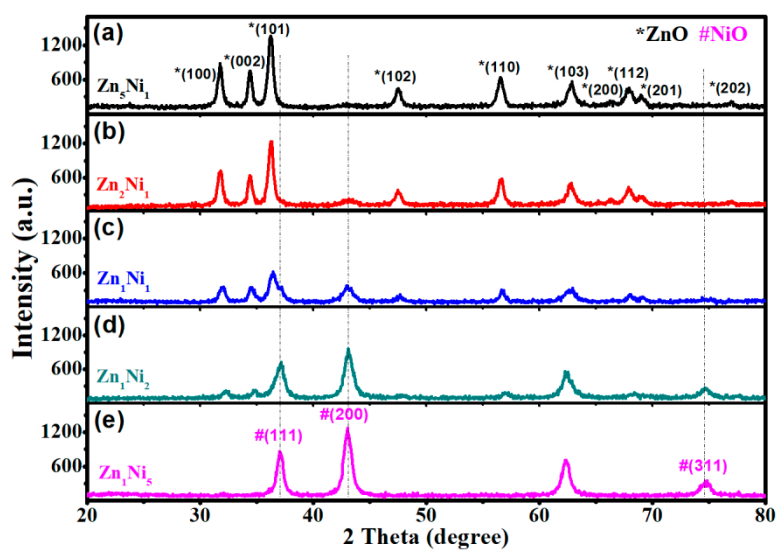


Figure 2. XRD patterns of the 3D *n*-ZnO/*p*-NiO hierarchical structures with the different molar ratios of Zn and Ni: Zn₅Ni₁ (a), Zn₂Ni₁ (b), Zn₁Ni₁ (c), Zn₁Ni₂ (d), and Zn₁Ni₅ (e).

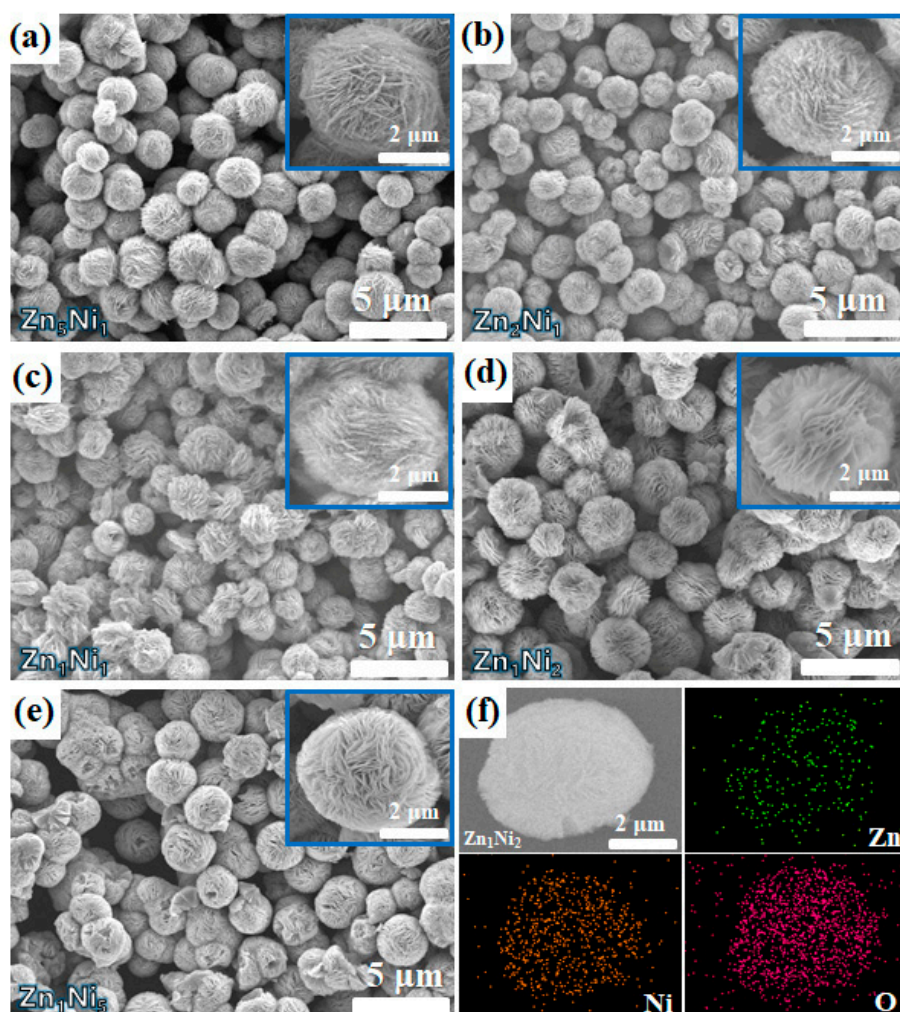


Figure 3. SEM images of as-prepared samples: Zn₅Ni₁ (a), Zn₂Ni₁ (b), Zn₁Ni₁ (c), Zn₁Ni₂ (d) and Zn₁Ni₅ (e). (f) The elemental mapping of Zn₁Ni₂ sample.

To clearly observe the morphology structure of as-synthesized *n*-ZnO/*p*-NiO hierarchical structure, transmission electron microscopy (TEM) analysis was conducted on the Zn_1Ni_2 sample. Figure 4a shows the morphological features at the boundary of nanosheets structure, which displays the uneven edges. The microstructure of Zn_1Ni_2 hierarchical structure was further studied by the high resolution-TEM (HRTEM). The measured lattice fringes presented in Figure 4b clearly exhibited two different spacings of approximately 0.21 and 0.28 nm, which can be assigned to the (200) plane of NiO and (100) plane of ZnO, respectively. Similarly, the interplanar distances of 0.24 and 0.25 nm agree well with the lattice spacing of the (111) plane of cubic NiO and (101) plane of hexagonal ZnO Figure 4c. Moreover, the selective area electron diffraction (SAED) pattern Figure 4d revealed that the diffraction rings can be indexed as the (100), (101), (110) planes of hexagonal ZnO and the (111), (220) planes of cubic NiO. Thus, the obtained TEM results were very consistent with previous XRD analysis and elemental mapping images, demonstrating that the 3D *n*-ZnO/*p*-NiO hierarchical structures have been successfully synthesized using hydrothermal method.

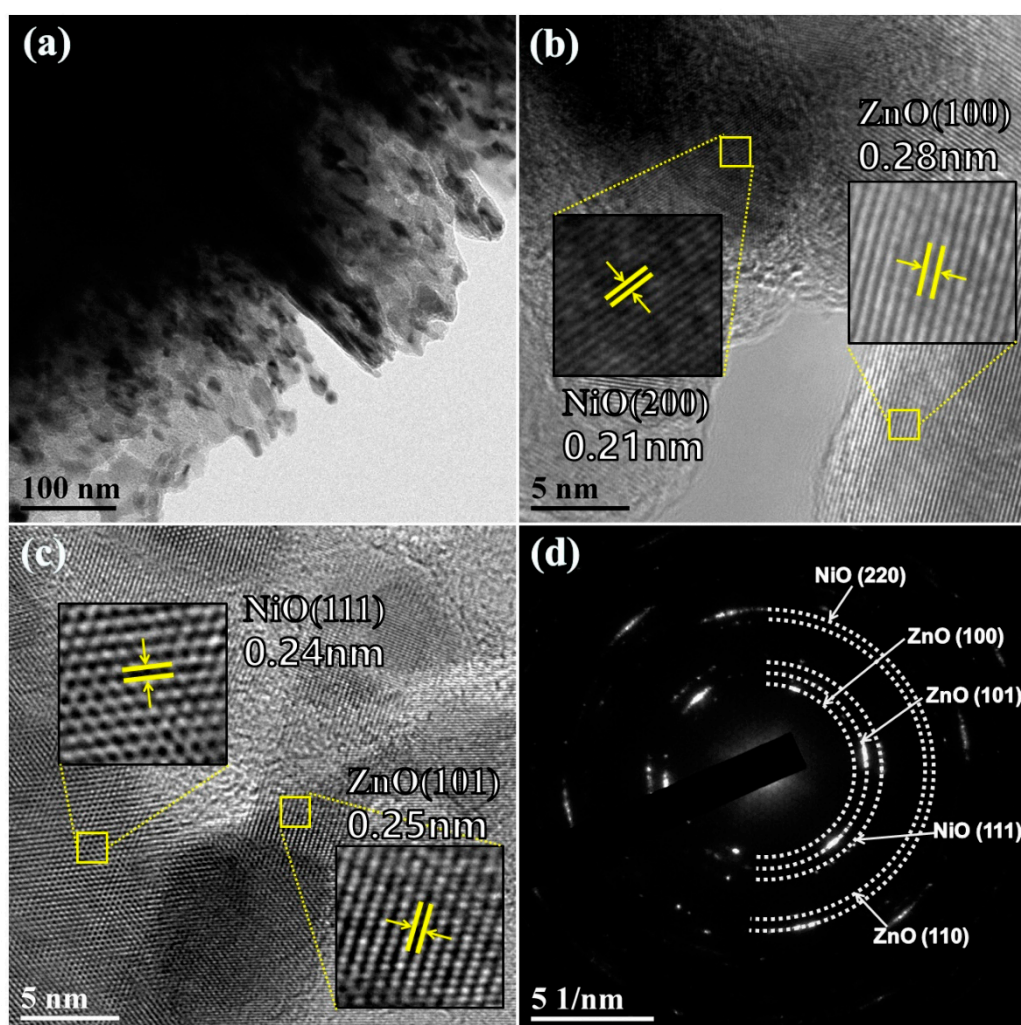


Figure 4. (a) Low resolution TEM image of Zn_1Ni_2 hierarchical structures. (b,c) High resolution TEM images of Zn_1Ni_2 hierarchical structures. (d) Selected area electron diffraction (SAED) patterns of Zn_1Ni_2 hierarchical structures.

Furthermore, to determine the elemental composition and chemical binding state of the Zn_1Ni_2 hierarchical structure, X-ray photoelectron spectroscopy (XPS) analysis was also carried out as shown in Figure 5. For the full range of XPS spectra Figure 5a, the binding energies corresponding to the different energy levels of Zn, Ni, O and C are evidently detected, and the binding energy at 284.6 eV of the C 1s is

used as a reference for calibration. Figure 5b displays the XPS spectra of Zn 2p, the measured spectrum shows two strong peaks with binding energy values of 1021.2 eV and 1044.3 eV, respectively, which can be assigned to Zn 2p_{3/2} and Zn 2p_{1/2} peaks [26]. Figure 5c shows the high-resolution spectrum of Ni 2p, including the characteristics peaks and the corresponding satellite peaks. The peaks located at 853.6 eV, 855.6 eV, and 861.1 eV are assigned to Ni 2p_{3/2} and its satellite peak. The higher binding energy located at 872.6 eV along with 879.1 eV can be attributed to Ni 2p_{1/2} and its corresponding satellite peak, which indicate the presence of Ni in the product [27,28]. Furthermore, the O 1s spectrum exhibits the two oxygen states of 529.5 eV and 531.2 eV Figure 5d. The lower binding energy peak corresponds to the lattice oxygen of O²⁻ in the oxide (ZnO, NiO), and the higher energy peak is associated with the chemisorbed oxygen species such as O⁻ and O₂⁻ [29].

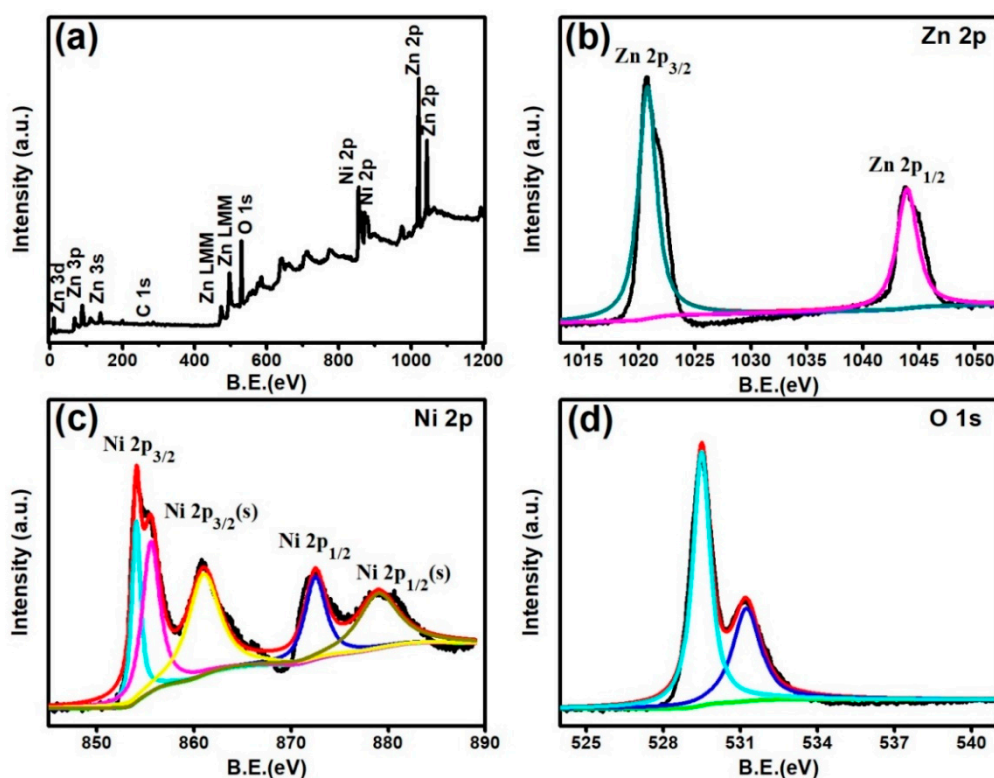


Figure 5. XPS survey spectra of Zn₁Ni₂ (a), high resolution spectra of Zn 2p (b), Ni 2p (c) and O 1s (d).

3.2. Gas Sensing Properties of Sensors

It is well-known that the sensor operating temperature can significantly influence its gas sensing properties [30], because it influences the process of oxygen adsorption and desorption on the sensing material. Hence, to optimize the sensor working temperature, gas sensing measurements were conducted on all the as-fabricated 3D Zn_xNi_y-based sensors toward 200 ppm NH₃ gas within the working temperature range of 160 to 340 °C, as presented in Figure 6a. Clearly, the gas sensing responses of Zn₅Ni₁, Zn₂Ni₁, Zn₁Ni₁ and Zn₁Ni₂ sensors increased to their maximum as the working temperature risen to 280 °C, and then decreased with further rise of the working temperature towards 340 °C. Thus, the optimum working temperature could be selected to be at 280 °C. The obtained phenomenon of the gas sensing performance was in good agreement with previous published works [31].

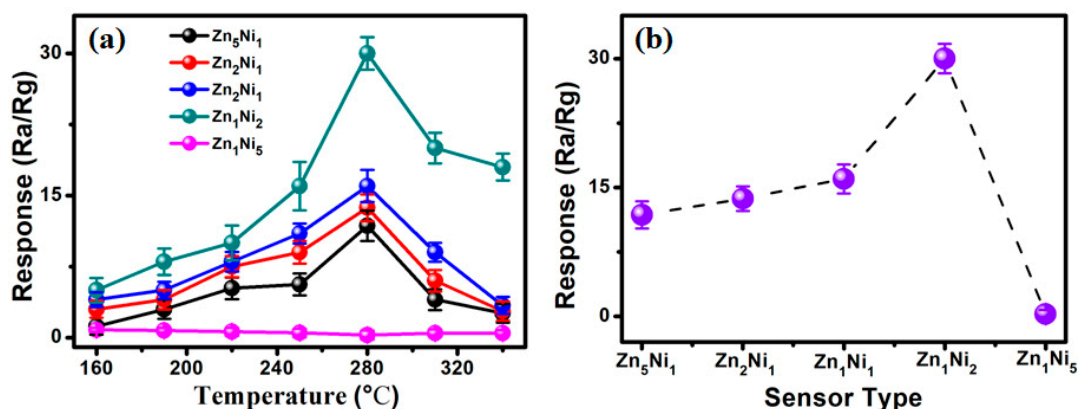


Figure 6. (a) Gas response of as-fabricated ZnO/NiO sensor toward 200 ppm NH₃ under different working temperatures. (b) Relationship of Response vs. Sensor type in presence of 200 ppm NH₃ at 280 °C.

However, for the Zn₁Ni₅ based sensor, Figure S1 (Supporting Information S1) clearly shows that the sensor response revealed the inverse tendency comparing with other *n*-ZnO/*p*-NiO based sensors within the working temperature range. We attributed the reason to the higher chemical composition of Ni element in Zn₁Ni₅ hierarchical nanostructures (as shown in Figure 2e), as it shows typical *p*-type response to NH₃ gas [32]. Furthermore, Figure 6b illustrates the response of all the as-developed 3D Zn_xNi_y-based sensors toward 200 ppm NH₃ at 280 °C. Obviously, the Zn₁Ni₂ sensor demonstrated the highest response of 31.2 toward 200 ppm NH₃, which is much higher than that of Zn₅Ni₁ (11.8), Zn₂Ni₁ (13.7), Zn₁Ni₁ (16) and Zn₁Ni₅ (0.26) based sensors. The obtained results unambiguously suggest that the appropriate Zn-to-Ni molar ratio is very advantageous for enhancement gas sensing performances of the 3D *n*-ZnO/*p*-NiO based sensor, and the as-developed Zn₁Ni₂ sensor displayed the best gas sensing property towards NH₃ sensing.

The dynamic gas sensing experiments were also conducted on the as-developed 3D Zn_xNi_y-based sensors to investigate their responses to the different NH₃ concentrations. Figure 7 depicts the sensor response to various NH₃ concentrations from 1 ppm to 300 ppm at the optimum working temperature (280 °C). Evidently, when gas sensors were exposed to 1 ppm of NH₃ gas, the sensor responses manifested increasing tendency for Zn₅Ni₁, Zn₂Ni₁, Zn₁Ni₁ and Zn₁Ni₂, as shown in Figure 7a. By successively injecting NH₃ gas with its concentration increasing from 1 ppm to 300 ppm, the sensor responses rose steeply, and then tended to a stable value, as well as exhibited appropriate step responses. Subsequently, when the 300 ppm of NH₃ was removed, their measured responses were quickly recovered to their initial response level, indicating that the as-prepared gas sensors based on 3D *n*-ZnO/*p*-NiO have good response-recovery characteristics. Particularly, the as-fabricated Zn₁Ni₂ sensor exhibited the superior dynamic response behavior compared to the other 3D Zn_xNi_y-based sensors. Moreover, the measured sensor responses of Zn₁Ni₂ sensor can reach to 6.1 (1 ppm), 8.0 (10 ppm), 10.7 (20 ppm), 15.2 (50 ppm), 24.9 (100 ppm), 34.2 (200 ppm) and 51.2 (300 ppm), respectively. On the other hand, Figure S2 (Supporting Information S2) illustrates the dynamic response of the Zn₁Ni₅ based sensor to NH₃ at the optimum working temperature (280 °C), and the amplification image revealed that the opposite response could be observed when the sensor was exposed to the different NH₃ concentrations. Consequently, the relationship between the gas responses and NH₃ concentrations were also presented for as-fabricated Zn_xNi_y sensors in Figure 7b. Compared with other 3D Zn_xNi_y hierarchical structures, the obtained results demonstrated that the sensor based on Zn₁Ni₂ hierarchical structure presents the maximum response under the same NH₃ concentration.

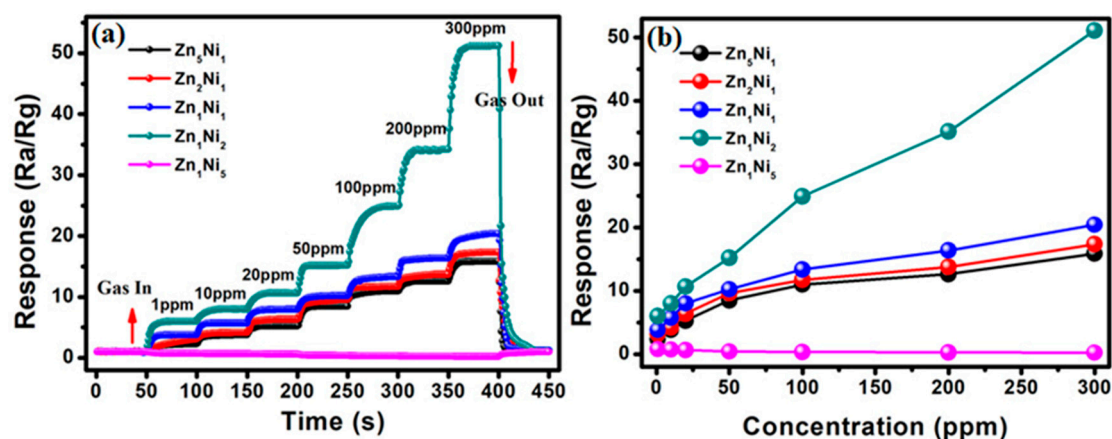


Figure 7. (a) Dynamic response of as-developed 3D *n*-ZnO/*p*-NiO based sensors toward high NH₃ concentration (1–300 ppm) at 280 °C. (b) Gas responses vs. NH₃ concentrations curves of ZnO/NiO sensors.

In order to further evaluate the gas sensing behavior of 3D *n*-ZnO/*p*-NiO based sensors toward the low concentrations of NH₃, the dynamic response-recovery characteristics of sensors were evaluated by their exposure to 50–500 ppb of NH₃ gas at the optimum working temperature of 280 °C. Figure 8a illustrates the real-time response curves of the 3D Zn_xNi_y based sensors toward 50 ppb, 100 ppb, 200 ppb, 300 ppb and 500 ppb target gases, and the sensor responses can recover to the baseline level when fresh air is injected, which suggests good response-recovery and reversibility for the low NH₃ concentrations at ppb level. Moreover, the obtained data confirmed that the Zn₁Ni₂ sensor still demonstrated better sensing capabilities than the other sensors, revealing its superior NH₃ sensing capacity even the ppb level. We speculated that the specific hierarchical nanosheet structure of the *n*-ZnO/*p*-NiO could produce much more contact sites on its surface. Thus, many NH₃ molecules will be adsorbed on the surface of the heterostructured sensing materials and oxidized by oxygen species at contact sites even at very low NH₃ concentration. Additionally, Figure 8b depicts the corresponding response of the linear relationships in logarithmic forms of the 3D Zn_xNi_y sensors (and the relationships of NH₃ concentration vs. response is shown in Figure S3 (Supporting Information S3)). The obtained relationship for the Zn₁Ni₂ sensor can be defined as the linear equation: $Y = 0.318 X + 0.06$ ($R^2 = 0.98$), and the slope of the straight line revealed that the sensor has high sensitivity even in the low concentrations of NH₃. Moreover, according to the measured experimental results, the linear correlation coefficients (R^2) are close to 1 for all the as-prepared 3D *n*-ZnO/*p*-NiO sensors, which indicated good linear relationships towards NH₃.

The response/recovery characteristic is one of the most important features for the NH₃ gas sensor for practical applications. Figure 9a–e represent the dynamic response and recovery curves of as-prepared Zn_xNi_y-based sensors toward 100 ppm NH₃ at the optimum working temperature of 280 °C. As summarized in Figure 9f, the measured response/recovery times (τ_{res}/τ_{rec}) of Zn₅Ni₁, Zn₂Ni₁, Zn₁Ni₁, Zn₁Ni₂ and Zn₁Ni₅ sensors were 6/8 s, 6/8 s, 12/8 s, 16/7 s and 6/18 s, respectively. Although the recovery time for Zn₁Ni₂ sensor was calculated to be about 16 s, the measured recovery time is only 7 s towards 100 ppm NH₃, which is a quite short recovery time among the as-developed *n*-ZnO/*p*-NiO sensors. Therefore, the obtained results demonstrated that the Zn₁Ni₂ sensor is indeed possesses good response-recovery characteristic for NH₃ detection. In addition, the sensing performance of the as-developed Zn₁Ni₂-based and most of the previously reported ZnO or NiO based NH₃ gas sensors are summarized in Table 1. When exposed to 100 ppm gas environment, the Zn₁Ni₂ sensor demonstrated outstanding sensitivity and response/recovery characteristics, as well as very low ppb detection limit.

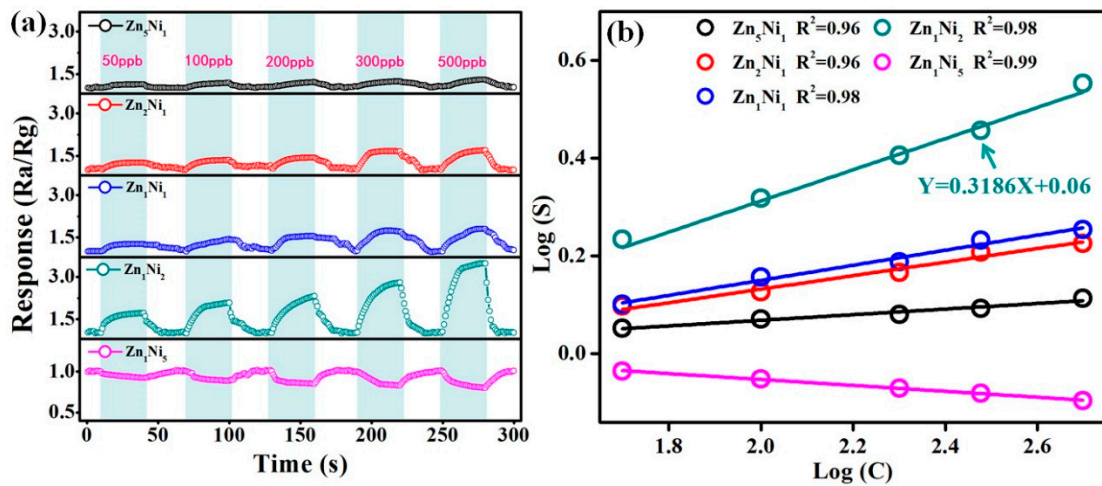


Figure 8. (a) Real-time response curves of 3D *n*-ZnO/*p*-NiO sensors toward the low NH₃ concentrations from 50 to 500 ppb at 280 °C. (b) Corresponding response of linear relationship with logarithmic forms of *n*-ZnO/*p*-NiO sensors.

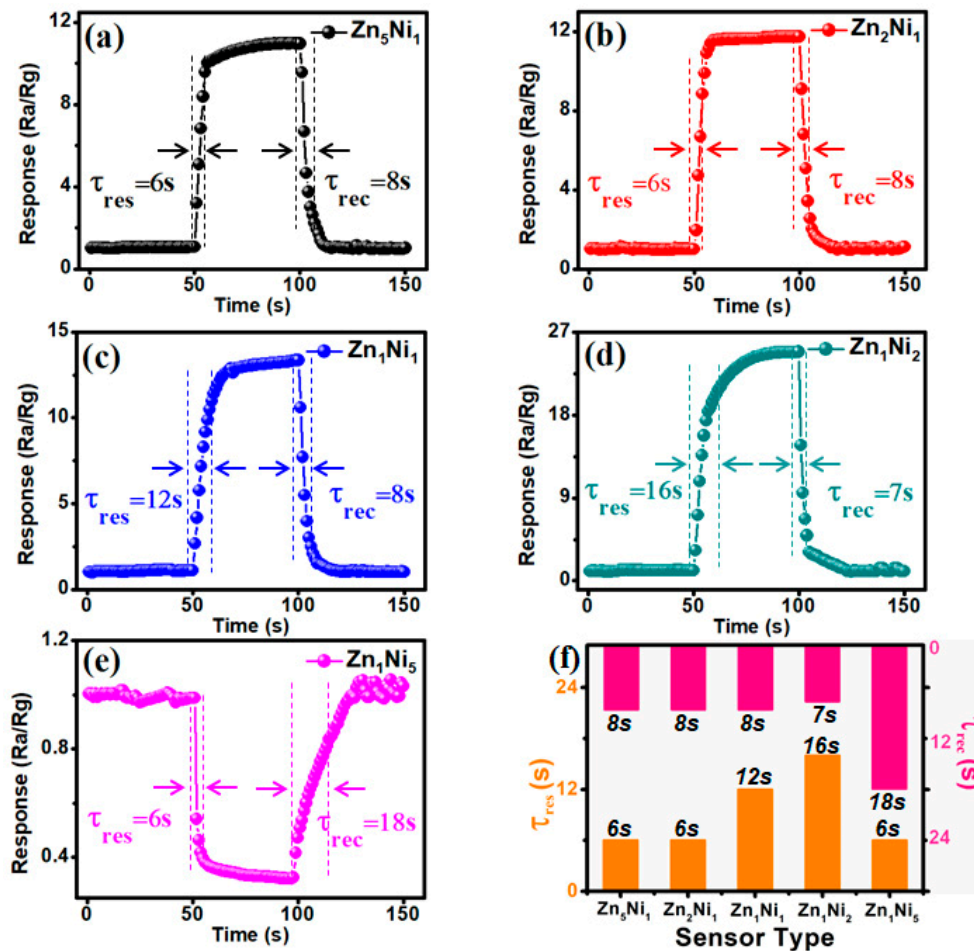


Figure 9. Dynamic sensing transient of *n*-ZnO/*p*-NiO based sensors toward 100 ppm NH₃: Zn_5Ni_1 (a), Zn_2Ni_1 (b), Zn_1Ni_1 (c), Zn_1Ni_2 (d) and Zn_1Ni_5 (e). (f) Response and recovery times of *n*-ZnO/*p*-NiO sensors.

Table 1. Comparison of the sensing performance of various gas sensors toward NH₃.

Sensing Materials	C (ppm)	T (°C)	Response	τ_{res}/τ_{rec} (s)	LOD (ppm)	Ref.
NiO	150	300	141.3%	-/-	25	[33]
NiO-MoS ₂	20	RT	79	160/117	0.25	[6]
Pt/NiO	1000	300	1278	15/76	0.01	[34]
ZnO nanorod	100	650	22.6	-/-	20	[35]
ZnO thin films	600	150	57.5	660/160	50	[36]
Co-ZnO	100	RT	3.48	-/-	15	[37]
3%Er-doped ZnO	120	RT	97%	120/10	–	[38]
ZnO-CNTs	50	RT	171(I_{gas}/I_{air})	18/35	0.2	[39]
CNTs/rGO/ZnO	10	RT	~2.25	55/116	5	[40]
WO ₃ /ZnO	300	250	25	60/50	25	[41]
ZnO/NiO nanofibers	100	RT	6	-/-	50	[42]
Zn ₁ Ni ₂	100	280	25	16/7	0.05	This work

C: Gas concentration; T: Operating temperature; τ_{res}/τ_{rec} : Response/recovery time; LOD: Limit of detection; RT: Room Temperature.

Figure 10a illustrates the selectivity test results for the Zn₁Ni₂ based NH₃ sensor, when it was exposed to 100 ppm of NH₃ and other potential interfering gases including 1-butanol (C₄H₁₀O), dichloromethane (CH₂Cl₂), ethanol (C₂H₆O), and methane (CH₄) at the optimal working temperature of 280 °C. The experimental results display that the Zn₁Ni₂ gas sensor exhibited the highest response (25) towards NH₃ compared with C₄H₁₀O (3.01), CH₂Cl₂ (1.55), C₂H₆O (2.22) and CH₄ (1.58), which demonstrates an excellent selectivity of the Zn₁Ni₂ sensor. In addition to selectivity, the repeatability is another important parameter for any gas sensor. Thus, Figure 10b shows another test result, when the sensors was consistently exposed to the cycling changes of NH₃ concentrations. It displays the response-recovery curve of the Zn₁Ni₂ sensor at the presence/absence of 50 ppm NH₃ for eight cycles at 280 °C. We can clearly observe that the sensor response maintains around 15 after the reversible cycles, illustrating good reversibility and reproducibility of the sensor performance.

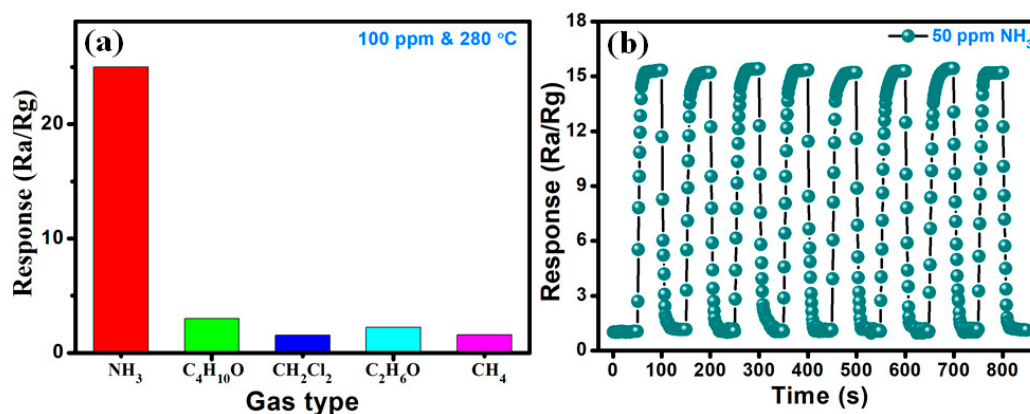


Figure 10. (a) Selectivity of Zn₁Ni₂ gas sensor toward various gases (100 ppm) at 280 °C. (b) Reversibility of Zn₁Ni₂ for 50 ppm NH₃.

Apart from investigation of selectivity and reproducibility characteristics, long-term stability of as-prepared *n*-ZnO/*p*-NiO based sensors was also investigated at the laboratory conditions. Figure 11 plots the collected response values when the sensors were exposed to 50 ppm NH₃ for 30 consecutive days. Obviously, there was no significant fluctuation in the response curves for the *n*-ZnO/*p*-NiO based sensors, and specifically, the response for Zn₁Ni₂ sensor showed only 5.0% fluctuation over 30 days, suggesting the good long-term stability for NH₃ detection.

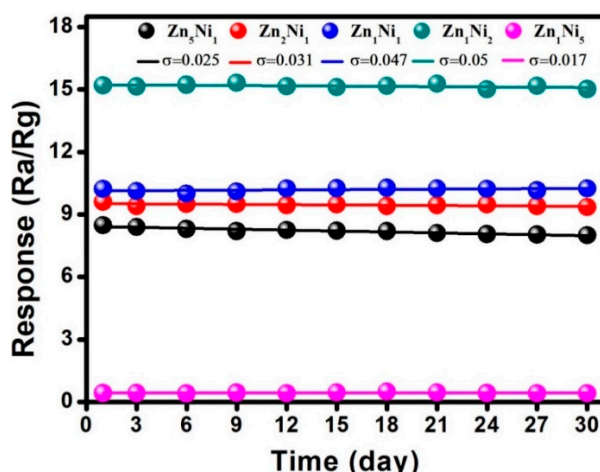


Figure 11. Long-term stability of as-prepared 3D *n*-ZnO/*p*-NiO based sensors toward 50 ppm NH₃ at 280 °C.

3.3. Gas Sensing Mechanism

For most of MOS-based gas sensors, the gas sensing mechanism can be explained by the resistance change on the surface of the sensing electrode material which is caused by adsorption and desorption of the target gas molecules [43]. The detailed sensing mechanism and the surface reaction of the 3D *n*-ZnO/*p*-NiO based sensor were depicted in Figure 12. When the as-prepared 3D *n*-ZnO/*p*-NiO sensor is exposed to air Figure 12a, the highly electronegative of oxygen molecules could be easily absorbed on the surface of sensing material by trapping free electrons, and then form different chemisorbed oxygen species (O⁻ in this experiment) under the various working temperatures (including O₂⁻ (T < 100 °C), O⁻ (100 < T < 300 °C), and O₂²⁻ (T > 300 °C) [44,45]. The loss of electrons will lead to a depletion layer and significantly increased resistance on the surface of *n*-type ZnO. In contrast, for the *p*-type NiO, the process will form a hole-accumulation layer and decrease the resistance. Their synergistic effect results in the change of sensor resistance. For instance, when NH₃ (reducing gas) is injected, O⁻ will react with NH₃ molecules and release electrons into the sensing electrode material, eventually leading to a resistance variation and sensing response Figure 12b. The gas sensing reaction for the *n*-ZnO/*p*-NiO hierarchical structures towards NH₃ detection can be described by the following equations:

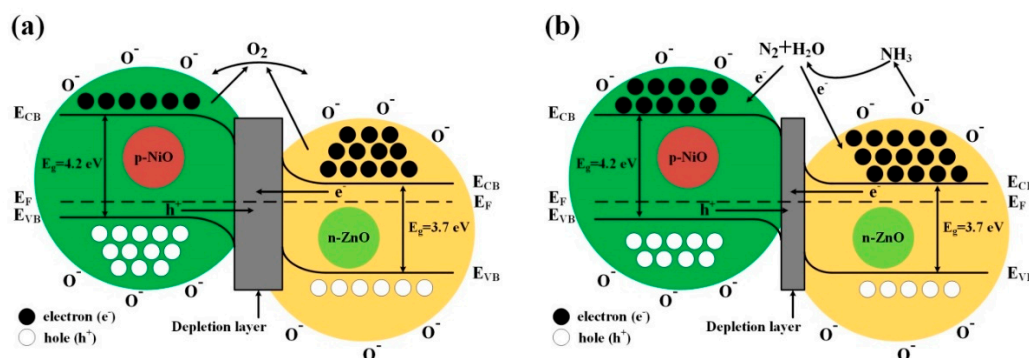
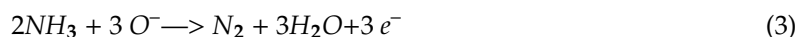


Figure 12. Proposed band structure model for 3D *n*-ZnO/*p*-NiO heterojunction (a) in air and (b) in NH₃. (E_{CB}, lower level of conduction band; E_F, Fermi level; E_{VB}, upper level of valence band).

Meanwhile, the excellent gas sensing properties of the *n*-ZnO/*p*-NiO gas sensor could be attributed to two aspects: on one hand, the morphological features exhibited the specific hierarchical nanosheets structure, which facilitated the adsorption of NH₃ molecules on the surface of hetero-structured sensing electrode and produces much more contact sites. On the other hand, the formation of *p*-*n* heterojunctions on the interface between the *n*-type ZnO and *p*-type NiO can contribute significantly to the improvement of the sensor responses. When the ZnO intimately contacts with the NiO, an internal self-built electrical field at the interface will be formed via charge carriers diffusion due to their different work functions, electron affinities and band gaps [46]. In the electrical field, the electrons transfer from ZnO to NiO, and holes move in the opposite direction until the systems achieve equalization at the Fermi level, as displayed in Figure S4 (Supporting Information S4) [24,47]. The process will lead to development of the potential barrier at the heterojunctions as the band bending and a wider depletion layer appears at their interface. For the Zn₁Ni₂ sample, it displays *n*-type semiconductor gas sensor which makes the electrons as majority carriers. These free electrons will be trapped by oxygen in air and lead to the increase of depletion layer width at *p*-*n* junction Figure 12a, thus it will further increase the resistance of the Zn₁Ni₂ than the pure ZnO. Correspondingly, the measured resistance of Zn₁Ni₂ will higher than pure ZnO. When the Zn₁Ni₂ sensor is exposed to NH₃ gas, the ammonia molecules will be oxidized by oxygen species and the trapped electrons will be released again. During the process, the depletion layer width at *p*-*n* junction is decreased and so that the resistance value drops drastically. Therefore, the depletion layer which formed at *p*-*n* junction is the main contributor to the best sensing performance of Zn₁Ni₂ sensor. Noteworthy, with the amount of NiO was increased, the gas sensor shown changes from *n*- to *p*-type transition. For example, for the *n*-type sensors (Zn₅Ni₁, Zn₂Ni₁, Zn₁Ni₁ and Zn₁Ni₂), the resistance will increase in air and decrease in NH₃, whereas for the *p*-type sensor (Zn₁Ni₅) the behavior is quite an opposite.

4. Conclusions

In summary, a series of 3D flower-like *n*-ZnO/*p*-NiO heterojunction composites with the different Zn-to-Ni ratios were synthesized (Zn_{*x*}Ni_{*y*}, *x*:*y* = 5:1, 2:1, 1:1, 1:2, 1:5) towards the development of sensing electrode with superior NH₃ sensing performance by a facile hydrothermal method. Their structural and morphological properties were comprehensively investigated by XRD, SEM, TEM and XPS techniques, confirming that the 3D flower-like *n*-ZnO/*p*-NiO structures were successfully created. The sensing performances of the Zn_{*x*}Ni_{*y*} heterostructures towards NH₃ sensing were analyzed under various working temperatures (160–340 °C) and showed different gas-sensing properties. Specifically, the fabricated NH₃ sensor based on Zn₁Ni₂ displayed the best sensing capabilities towards NH₃ detection at the established optimum working temperature of 280 °C. Moreover, this sensor exhibited the high response of 25 and fast response/recovery time of 16 s/7 s toward 100 ppm NH₃, as well as the low detection limit of 50 ppb, good selectivity and long-term stability. Therefore, the present study has successfully demonstrated the vital role of the *p*-*n* heterojunctions for the enhancement of gas sensing properties, confirmed that the 3D *n*-ZnO/*p*-NiO nanocomposites are sensing material candidate for constructing NH₃ sensors with promising application.

Supplementary Materials: The following are available online at <http://www.mdpi.com/1424-8220/20/17/4754/s1>, Figure S1: Gas response of the Zn₁Ni₅ toward 200 ppm NH₃ under the different working temperatures, Figure S2: Dynamic response of the Zn₁Ni₅ to 1–300 ppm concentrations of NH₃ at 280 °C, Figure S3: Response of the 3D *n*-ZnO/*p*-NiO with the different Zn-to-Ni molar ratio to 50–500 ppb NH₃ concentrations at 280 °C, Figure S4: Energy band structure of *p*-type NiO and *n*-type ZnO before and after contact.

Author Contributions: Conceptualization, Z.Z., S.Z. and J.H.; methodology, Z.Z., Y.X., H.Y. and J.H.; software, Y.X. and H.Y.; validation, Z.W. and Y.X.; formal analysis, Z.Z.; investigation, Z.Z. and Y.X.; resources, Z.Z.; data curation, W.Z. and P.L.; writing—original draft preparation, Z.Z. and Y.X.; writing—review and editing, Z.Z., H.Y., Z.W., W.G. and S.Z.; visualization, Z.Z., Y.S. and J.H.; supervision, J.H.; project administration, Z.Z. and J.H.; funding acquisition, Z.Z. and J.H.. All authors have read and agreed to the published version of the manuscript.

Funding: This work was financially supported by the National Natural Science Foundation of China (61901186), the special innovation projects of universities in Guangdong province (2019KTSCX178), the Program for Innovative

Research Team of Huizhou University (IRTHZU), and the Open Project Program of Guangdong Provincial Key Laboratory of Electronic Functional Materials and Devices, Huizhou University (No. EFMD2020002Z).

Conflicts of Interest: The authors declare no conflict of interest.

References

1. Mukhopadhyaya, T.; Wagner, J.S.; Fan, H.; Katz, H.E. Design and synthesis of air-stable p-channel-conjugated polymers for high signal-to-drift nitrogen dioxide and ammonia sensing. *ACS Appl. Mater. Interfaces* **2020**, *12*, 21974–21984. [[CrossRef](#)] [[PubMed](#)]
2. Kwak, D.; Lei, Y.; Maric, R. Ammonia gas sensors: A comprehensive review. *Talanta* **2019**, *204*, 713–730. [[CrossRef](#)] [[PubMed](#)]
3. Smith, A.F.; Liu, X.; Woodard, T.L.; Fu, T.; Emrick, T.; Jimenez, J.M.; Lovley, D.R.; Yao, J. Bioelectronic protein nanowire sensors for ammonia detection. *Nano Res.* **2020**, *13*, 1749–1848. [[CrossRef](#)]
4. Deng, Z.; Meng, G.; Fang, X.; Dong, W.; Shao, J.; Wang, S.; Tong, B. A novel ammonia gas sensors based on p-type delafossite AgAlO₂. *J. Alloy. Compd.* **2019**, *777*, 52–58. [[CrossRef](#)]
5. Wong, D.; Abuzalat, O.; Mostafa, S.; Park, S.S.; Kim, S. Intense pulsed light-based synthesis of hybrid TiO₂-SnO₂/MWCNT doped Cu-BTC for room temperature ammonia sensing. *J. Mater. Chem. C* **2020**, *8*, 7567. [[CrossRef](#)]
6. Zhang, D.; Jin, Y.; Cao, Y. Facile synthesis and ammonia gas sensing properties of NiO nanoparticles decorated MoS₂ nanosheets heterostructure. *J. Mater. Sci.* **2019**, *30*, 573–581. [[CrossRef](#)]
7. Benamara, M.; Massoudi, J.; Dahman, H.; Dhahri, E.; El Mir, L.; Ly, A.; Debliquy, M.; Lahem, D. High response to sub-ppm level of NO(2) with 50%RH of ZnO sensor obtained by an auto-combustion method. *J. Mater. Sci.* **2020**. [[CrossRef](#)]
8. Hiyoto, K.A.M.; Fisher, E.R. Utilizing plasma modified SnO₂ paper gas sensors to better understand gas-surface interactions at low temperatures. *J. Vac. Sci. Technol. A* **2020**, *38*, 043202. [[CrossRef](#)]
9. Mokoena, T.P.; Tshabalala, Z.P.; Hillie, K.T.; Swart, H.C.; Motaung, D.E.; Shen, Y.B. The blue luminescence of p-type NiO nanostructured material induced by defects: H₂S gas sensing characteristics at a relatively low operating temperature. *App. Surf. Sci.* **2020**, *525*, 146002. [[CrossRef](#)]
10. Büyükköse, S. Highly selective and sensitive WO₃ nanoflakes based ammonia sensor. *Mat. Sci. Semicon. Proc.* **2020**, *110*, 104969. [[CrossRef](#)]
11. Addabbo, T.; Bruzzi, M.; Fort, A.; Mugnaini, M.; Vignoli, V. Gas sensing properties of In₂O₃ nano-films obtained by low temperature pulsed electron deposition technique on alumina substrates. *Sensors* **2018**, *18*, 4410. [[CrossRef](#)] [[PubMed](#)]
12. Zhang, J.; Qin, Z.; Zeng, D.; Xie, C. Metal-oxide-semiconductor based gas sensors: Screening, preparation, and integration. *Phys. Chem. Chem. Phys.* **2017**, *19*, 6313–6329. [[CrossRef](#)] [[PubMed](#)]
13. Pang, Z.; Nie, Q.; Zhu, Y.; Ge, M.; Chen, M. Enhanced ammonia sensing characteristics of CeO₂-decorated SiO₂/PANI free-standing nanofibrous membranes. *J. Mater. Sci.* **2019**, *54*, 2333–2342. [[CrossRef](#)]
14. Sun, Y.; Wei, Z.; Zhang, W.; Li, P.; Lian, K.; Hu, J. Synthesis of brush-like ZnO nanowires and their enhanced gas-sensing properties. *J. Mater. Sci.* **2016**, *51*, 1428–1436. [[CrossRef](#)]
15. Parellada-Monreal, L.; Gherardi, S.; Zonta, G.; Malagu, C.; Casotti, D.; Cruciani, G.; Guidi, V.; Martinez-Calderon, M.; Castro-Hurtado, I.; Gamarra, D. WO₃ processed by direct laser interference patterning for NO₂ detection. *Sens. Actuators B Chem.* **2020**, *305*, 127226. [[CrossRef](#)]
16. Castillo, C.; Cabello, G.; Chornik, B.; Huentupil, Y.; Buono-Core, G.E. Characterization of photochemically grown Pd loaded WO₃ thin films and its evaluation as ammonia gas sensor. *J. Alloy. Compd.* **2020**, *825*, 154166. [[CrossRef](#)]
17. Sanger, A.; Kumar, A.; Kumar, A.; Jaiswal, J.; Chandra, R. A fast response/recovery of hydrophobic Pd/V₂O₅ thin films for hydrogen gas sensing. *Sens. Actuators B Chem.* **2016**, *236*, 16–26. [[CrossRef](#)]
18. Nakate, U.T.; Ahmad, R.; Patil, P.; Wang, Y.; Bhat, K.S.; Mahmoudi, T.; Yu, Y.T.; Suh, E.; Hahn, Y.B. Improved selectivity and low concentration hydrogen gas sensor application of Pd sensitized heterojunction n-ZnO/p-NiO nanostructures. *J. Alloy. Compd.* **2019**, *797*, 456–464. [[CrossRef](#)]
19. Zhang, S.; Li, Y.; Sun, G.; Zhang, B.; Wang, Y.; Gao, J.; Zhang, Z. Synthesis of NiO-decorated ZnO porous nanosheets with improved CH₄ sensing performance. *Appl. Surf. Sci.* **2019**, *497*, 143811. [[CrossRef](#)]

20. Liu, Y.; Li, G.; Mi, R.; Deng, C.; Gao, P. An environment-benign method for the synthesis of p-NiO/n-ZnO heterostructure with excellent performance for gas sensing and photocatalysis. *Sens. Actuators B Chem.* **2014**, *191*, 537–544. [[CrossRef](#)]
21. Krishnakumar, T.; Kiruthiga, A.; Jozwiat, E.; Moulalee, K.; Neri, G. Development of ZnO-based sensors for fuel cell cars equipped with ethanol steam-reformer for on-board hydrogen production. *Ceram. Int.* **2020**, *46*, 17076–17084. [[CrossRef](#)]
22. Alev, O.; Sarica, N.; Ozdemir, O.; Arslan, L.C.; Buyukkose, S.; Ozturk, Z.Z. Cu-doped ZnO nanorods based QCM sensor for hazardous gases. *J. Alloy. Compd.* **2020**, *826*, 154177. [[CrossRef](#)]
23. Chen, H.J.; Bo, R.H.; Shrestha, A.; Xin, B.B.; Nasiri, N.; Zhou, J.; Di Bernardo, I.; Dodd, A.; Saunders, M.; Lipton-Duffin, J. NiO-ZnO nanoheterojunction networks for room-temperature volatile organic compounds sensing. *Adv. Opt. Mater.* **2018**, *6*, 1800677. [[CrossRef](#)]
24. Kaur, N.; Zappa, D.; Ferroni, M.; Poli, N.; Campanini, M.; Negrea, R.; Comini, E. Branch-like NiO/ZnO heterostructures for VOC sensing. *Sens. Actuators B Chem.* **2018**, *262*, 477–485. [[CrossRef](#)]
25. Zhou, Q.; Zeng, W.; Chen, W.; Xu, L.; Kumar, R.; Umar, A. High sensitivity and low-concentration sulfur dioxide (SO₂) gas sensor application of heterostructure NiO-ZnO nanodisks. *Sens. Actuators B Chem.* **2019**, *298*, 126870. [[CrossRef](#)]
26. Fouad, F.A.; Ahmed, M.A.; Antonious, M.S.; Abdel-Messih, M.F. Synthesis of an efficient, stable and recyclable AgVO₃/ZnO nanocomposites with mixed crystalline phases for photocatalytic removal of rhodamine B dye. *J. Mater. Sci.* **2020**, *31*, 12355–12371. [[CrossRef](#)]
27. Lontio Fomekong, R.; Tedjiekeng Kamta, H.M.; Ngolui Lambi, J.; Lahem, D.; Eloy, P.; Debliquy, M.; Delcorte, A. A sub-ppm level formaldehyde gas sensor based on Zn-doped NiO prepared by a coprecipitation route. *J. Alloy. Compd.* **2018**, *731*, 1188–1196. [[CrossRef](#)]
28. Reddy, K.C.S.; Sahatiya, P.; Santos-Sauceda, I.; Cortazar, O.; Ramirez-Bon, R. One-step fabrication of 1D p-NiO nanowire/n-Si heterojunction: Development of self-powered ultraviolet photodetector. *Appl. Surf. Sci.* **2020**, *513*, 145804. [[CrossRef](#)]
29. Rai, P.; Yoon, J.W.; Kwak, C.H.; Lee, J.H. Role of Pd nanoparticles in gas sensing behaviour of Pd@In₂O₃ yolk-shell nanoreactors. *J. Mater. Chem. A* **2016**, *4*, 264–269. [[CrossRef](#)]
30. Sun, G.J.; Kheel, H.; Park, S.; Lee, S.; Park, S.; Lee, C. Synthesis of TiO₂ nanorods decorated with NiO nanoparticles and their acetone sensing properties. *Ceram. Int.* **2016**, *42*, 1063–1069. [[CrossRef](#)]
31. Kim, J.H.; Lee, J.H.; Mirzaei, A.; Kim, H.W.; Kim, S.S. SnO₂ (n)-NiO (p) composite nanowires: Gas sensing properties and sensing mechanisms. *Sens. Actuators B Chem.* **2018**, *258*, 204–214. [[CrossRef](#)]
32. Wang, J.; Zhou, Y.L.; Zhou, H.T.; Wangyang, Q.Y.; Peng, Y.J.; Wangyang, P.H.; Gu, L. Durian-like NiO architectures as an ultra-sensitive sensing materials for ammonia in normal temperature. *Ceram. Int.* **2018**, *45*, 1219–1226. [[CrossRef](#)]
33. Gomaa, M.M.; RezaYazdi, G.; Rodner, M.; Greczynski, G.; Boshta, M.; Osman, M.B.S.; Khranovskyy, V.; Eriksson, J.; Yakimova, R. Exploring NiO nanosize structures for ammonia sensing. *J. Mater. Sci.* **2018**, *29*, 11870–11877. [[CrossRef](#)]
34. Chen, H.I.; Hsiao, C.Y.; Chen, W.C.; Chang, C.; Chou, T.; Liu, I.; Lin, K.; Liu, W. Characteristics of a Pt/NiO thin film-based ammonia gas sensor. *Sens. Actuators B Chem.* **2018**, *256*, 962–967. [[CrossRef](#)]
35. Anantachaisilp, S.; Smith, S.M.; Ton-that, C.; Osotchan, T.; Moon, A.R.; Phillips, M.R. Tailoring Deep Level Surface Defects in ZnO Nanorods for High Sensitivity Ammonia Gas Sensing. *J. Phys. Chem. C* **2014**, *118*, 27150–27156. [[CrossRef](#)]
36. Li, C.F.; Hsu, C.Y.; Li, Y.Y. NH₃ sensing properties of ZnO thin films prepared via sol-gel method. *J. Alloy. Compd.* **2014**, *606*, 27–31. [[CrossRef](#)]
37. Mani, G.K.; Rayappan, J.B.B. A highly selective and wide range ammonia sensor-Nanostructured ZnO:Co thin film. *Mater. Sci. Eng. B* **2015**, *191*, 41–50. [[CrossRef](#)]
38. Deva Arun Kumar, K.; Valanarasu, S.; Ponraj, J.S.; Fernandes, B.J.; Shkir, M.; AlFaify, S.; Murahari, P.; Ramesh, K. Effect of Er doping on the ammonia sensing properties of ZnO thin films prepared by a nebulizer spray technique. *J. Phys. Chem. Solids* **2020**, *144*, 109513. [[CrossRef](#)]
39. Schutt, F.; Postica, V.; Adelung, R.; Lupan, O. Single and networked ZnO-CNT hybrid tetrapods for selective room-temperature high-performance ammonia sensors. *ACS Appl. Mater. Interfaces* **2017**, *9*, 23107–23118. [[CrossRef](#)]

40. Morsy, M.; Yahia, I.S.; Zahran, H.Y.; Meng, F.; Ibrahim, M. Portable and battery operated ammonia gas sensor based on CNTs/rGO/ZnO nanocomposite. *J. Electron. Mater.* **2019**, *48*, 7328–7335. [[CrossRef](#)]
41. Nguyen, D.D.; Do, D.T.; Vu, X.H.; Dang, D.V.; Nguyen, D.C. ZnO nanoplates surfaced-decorated by WO₃ nanorods for NH₃ gas sensing application. *Adv. Nat. Sci. Nanosci.* **2016**, *7*, 015004. [[CrossRef](#)]
42. Lokesh, K.; Kavitha, G.; Manikandan, E.; Mani, G.K.; Kaviyarasu, K.; Rayappan, J.B.B.; Ladchumananandasivam, R.; Aanand, J.S.; Jayachandran, M.; Maaza, M. Effective ammonia detection using n-ZnO/p-NiO heterostructured nanofibers. *IEEE Sens. J.* **2016**, *16*, 2477–2483. [[CrossRef](#)]
43. Li, C.; Feng, C.; Qu, F.; Liu, J.; Zhu, L.; Lin, Y.; Wang, Y.; Li, F.; Zhou, J.; Ruan, S. Electrospun nanofibers of p-type NiO/n-type ZnO heterojunction with different NiO content and its influence on trimethylamine sensing properties. *Sens. Actuators B Chem.* **2015**, *207*, 90–96. [[CrossRef](#)]
44. San, X.; Li, M.; Liu, D.; Wang, G.; Shen, Y.; Meng, D.; Meng, F. A facile one-step hydrothermal synthesis of NiO/ZnO heterojunction microflowers for the enhanced formaldehyde sensing properties. *J. Alloy. Compd.* **2018**, *739*, 260–269. [[CrossRef](#)]
45. Kim, J.H.; Lee, J.H.; Mirzaei, A.; Kim, H.W.; Kim, S.S. Optimization and gas sensing mechanism of n-SnO₂-p-Co₃O₄ composite nanofibers. *Sens. Actuators B Chem.* **2017**, *248*, 500–511. [[CrossRef](#)]
46. Zhu, L.; Zeng, W.; Yang, J.; Li, Y. One-step hydrothermal fabrication of nanosheet-assembled NiO/ZnO microflower and its ethanol sensing property. *Ceram. Int.* **2018**, *44*, 19825–19830. [[CrossRef](#)]
47. Jayababu, N.; Poloju, M.; Shruthi, J.; Ramana Reddy, M.V. Synthesis of ZnO/NiO nanocomposites for the rapid detection of ammonia at room temperature. *Mat. Sci. Semicon. Proc.* **2019**, *102*, 104591. [[CrossRef](#)]



© 2020 by the authors. Licensee MDPI, Basel, Switzerland. This article is an open access article distributed under the terms and conditions of the Creative Commons Attribution (CC BY) license (<http://creativecommons.org/licenses/by/4.0/>).